Chemical Engineering Journal 359 (2019) 79–87

Contents lists available at ScienceDirect

Chemical Engineering Journal

journal homepage: www.elsevier.com/locate/cej

Cobalt silicate hydroxide nanosheets in hierarchical hollow architecture with maximized cobalt active site for catalytic oxidation

Penghui Shao[a], Jiayu Tian[b,*], Xiaoguang Duan[c], Yi Yang[d], Wenxin Shi[e], Xubiao Luo[a,*], Fuyi Cui[e], Shenglian Luo[a], Shaobin Wang[c,*]

[a] Key Laboratory of Jiangxi Province for Persistent Pollutants Control and Resources Recycle, Nanchang Hangkong University, Nanchang 330063, PR China
[b] School of Civil Engineering and Transportation, Hebei University of Technology, Tianjin 300401, PR China
[c] School of Chemical Engineering, The University of Adelaide, Adelaide, SA 5005, Australia
[d] Beijing Urban Construction Design and Development Group Co Ltd, Beijing 100032, PR China
[e] College of Urban Construction and Environmental Engineering, Chongqing University, Chongqing 400044, PR China

HIGHLIGHTS

- Cobalt silicate hydroxide in hierarchical hollow nanospheres (CSH) were synthesized.
- CSH-80 exhibited outstanding catalytic performance and excellent stability.
- High cobalt site number and TOF were achieved in CSH-80@PMS system.
- $SO_4^{\cdot -}$ rather than $\cdot OH/^1O_2$ dominated the degradation of organic contaminants.

GRAPHICAL ABSTRACT

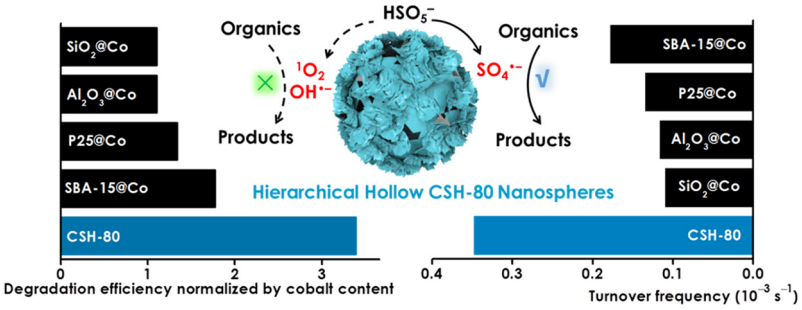

ARTICLE INFO

Keywords:
Peroxymonosulfate
Cobalt-based catalyst
Utilization efficiency
Cobalt silicate hydroxide
Organic pollutant

ABSTRACT

A facile dissolution-regrowth strategy was developed in synthesis of hierarchical hollow nanospheres of cobalt silicate hydroxide (CSH-80) for maximizing cobalt active sites on unit mass basis, which is different from the conventional supported cobalt catalysts. Due to the unique design and elaborative nanoarchitecture, the cobalt active center can be homogeneously dispersed into the structured catalyst, achieving the maximum exposure of the cobalt center for reaction. In activation of peroxymonosulfate (PMS) for degradation of organic contaminants, CSH-80 exhibited outstanding catalytic performance, excellent physicochemical stability and long-term durability, giving 1.9–3.1 folds higher efficiency than that of the conventional supported cobalt catalysts. The turnover frequency of CSH-80 in organic oxidation was 2.0–3.2 folds higher than that of the conventional supported cobalt catalysts. The effects of reaction parameters on contaminant degradation were systematically investigated. The catalytic oxidation mechanism was further elucidated by the quenching tests, electron paramagnetic resonance and photoluminescence studies. The design concept in this study will provide new opportunities for future development of high-performance cobalt-based heterogeneous catalysts in environmental remediation.

* Corresponding authors.
E-mail addresses: tjy800112@163.com (J. Tian), luoxubiao@126.com (X. Luo), shaobin.wang@adelaide.edu.au (S. Wang).

https://doi.org/10.1016/j.cej.2018.11.121
Received 28 August 2018; Received in revised form 14 November 2018; Accepted 16 November 2018
Available online 16 November 2018
1385-8947/

1. Introduction

Advanced oxidation processes (AOPs) are state of the art technologies for elimination of organic contaminants in wastewater, especially for the refractory and non-biodegradable pollutants [1–4]. Sulfate radical ($SO_4^{\bullet-}$)-based AOPs have attracted increasing attention in recent years owing to the unique properties of $SO_4^{\bullet-}$, such as a higher redox potential (2.5–3.1 V), longer half-life (30–40 μs) and selectivity to target pollutants compared with hydroxyl radical (•OH) [5–11]. It is well known that homogeneous catalytic reaction of transition metal ions with peroxymonosulfate (PMS) is a highly efficient approach to generate $SO_4^{\bullet-}$, and Co^{2+} ions are the best activators. Additionally, Co^{2+}/PMS has been revealed to be more efficient than the classical Fenton system for degradation of organic pollutants [12]. Despite that the homogeneous catalytic system possesses a superior oxidative capacity, Co^{2+} ions are very difficult to be recovered for reuse. Hence, the discharge of cobalt-containing water will lead to an adverse effect on aquatic environment, which significantly impedes its practical applications in water treatment.

To avoid the inherent disadvantages of homogeneous catalysis, researchers have developed cobalt-based heterogeneous catalysts. Various substrate materials have been exploited for immobilization of active cobalt species [6,13–15]. For example, Zeng et al. synthesized nanocomposites of yolk-shell Co_3O_4@metal-organic-frameworks (MOFs) with a void cavity between the catalytically active Co_3O_4 core and uniform octahedral MOFs shell. Benefiting from its unique nanostructure, the Co_3O_4@MOFs nanocomposites exhibited improved catalytic activity and stability in PMS activation for 4-chlorophenol degradation [16]. In another study, a $Co(OH)_2$ nanoflake-reduced graphene oxide (rGO) hybrid was synthesized by a one-pot hydrothermal method. The as-synthesized nano-hybrids showed a much improved reactivity than sole $Co(OH)_2$ or rGO [17].

Although cobalt-based heterogeneous catalysts circumvented the limitations of cobalt ion-based homogenous catalysis, the effective cobalt site in these heterogeneous catalysts is rather low on unit mass basis. Generally, cobalt oxides anchored on supported materials are typically solid nanoparticles (NPs) with an irregular outline whereas the catalytic reaction occurs only on the surface, leading to a huge waste of cobalt in the bulk. On the other hand, cobalt oxide NPs tend to be assembled into the large aggregations due to its high surface energy, resulting in a significant decrease of the accessible surface area of the NPs. As a result, further reduction in the cobalt catalytic efficiency was inevitably suffered. Therefore, rational design and controllable synthesis of a supported cobalt catalyst is highly desirable to inherit the high efficiency of homogeneous catalysis in a heterogeneous system.

The aforementioned issue suggests that an ideal cobalt-based heterogeneous catalyst may follow some protocols in regard to the structural designs. First, the active cobalt center should be homogeneously dispersed onto the entire structure of the catalyst, behaving like Co^{2+} ions homogeneously dissolved in water. Secondly, the specific surface area (SSA) and pore volume of the catalyst should be high in order to expose the active centers to the maximum level. Thirdly, the catalyst should have outstanding physicochemical stability. Toward this, a facile dissolution-regrowth strategy was developed in the present study for synthesis of cobalt silicate hydroxide (CSH) in hierarchical hollow nanospheres with ultrathin nanosheets. Owing to its unique design and elaborative nanoarchitecture, the active cobalt centers were homogeneously dispersed within the entire materials. The optimal exposure of the cobalt centers can be realized. An as-synthesized CSH-80 exhibited outstanding catalytic activity and excellent stability in activation of PMS for oxidation of organic contaminants in water. More importantly, the cobalt catalytic efficiency of CSH-80 is much higher (1.9–3.1 folds) than that of the conventional supported Co catalysts on the basis of unit mass. Correspondingly, the turnover frequency (TOF) of CSH-80 catalyzed RhB oxidation was 2.0–3.2 folds higher than that of the conventional supported cobalt catalysts.

2. Experimental section

2.1. Chemicals

The chemicals, 5,5-dimethyl-pyrroline-oxide (DMPO, ≥97%), *tert*-butyl alcohol (TBA, ≥99%), methanol (≥99.9%), benzoic acid (BA, 98%), atrazine (ATZ, 99%), furfuryl alcohol (FFA, 98%), humic acid, sulfamethoxazole (SMX, analytical standard), and sodium azide (NaN_3, 99.5%) were purchased from Sigma-Aldrich. Bisphenol S (BPS, >98%) and bisphenol F (BPF, >98%) were purchased from TCI. 2,2,6,6-Tetramethyl-4-piperidinol (TMP, 99%) was purchased from J&K Scientific Co. Cobalt(III) acetylacetonate ($Co(acac)_3$, 98%), rhodamine B (RhB, 95%), tetraethyl orthosilicate (TEOS, 98%), peroxymonosulfate (PMS, ≥47% $KHSO_5$ basis), Co_3O_4 NPs (~100 nm, 99%), CuO NPs (~40 nm, 99%), and 4-chlorophenol (4-CP, 99%) were purchased from Aladdin Co. Other chemicals in analytical grade or better were purchased from Sinopharm Chemical Reagent Co.

2.2. Synthesis of catalysts

SiO_2 nanospheres were first prepared by the classic Stöber method with minor modifications (Supporting Information). For synthesis of cobalt silicate hydroxide, a given mass of SiO_2 nanospheres (20–80 mg) were dispersed in 70 mL deionized water for 0.5 h. Then, 100 mg of Co $(acac)_3$ was added under stirring for 1.0 h. After that, the above suspensions were transferred into a Teflon-lined autoclave, which was sealed and maintained at 180 °C for 12 h. The obtained precipitate was collected by centrifugation and washed several times with absolute ethanol and deionized water. Finally, the synthesized samples were dried in an oven at 50 °C overnight. For synthesis of other Co-supported catalysts, a usual dipping-annealing method was employed as shown in Supporting Information.

2.3. Characterizations

Micro-morphologies of the samples were observed using a JEOL JEM-1400 transmission electron microscope (TEM). X-ray diffraction (XRD) patterns were collected from a Bruker D8 X-ray diffractometer with Cu Kα radiation (λ = 0.15418 nm). The Brunauer-Emmett-Teller (BET) surface area measurements were performed on an ASAP2020 instrument. X-ray photoelectron spectroscopy (XPS) measurements were performed using a Thermo ESCALAB 250 with Al Kα X-ray radiation ($h\nu$ = 1486.6 eV). Fourier transform-infrared (FTIR) spectra were recorded on a Perkin-Elmer Spectrum One B spectrometer. For the analysis of cobalt of contents, the samples were digested by strong acid and measured by an inductively coupled plasma-optical emission spectrometer (ICP-OES, Perkin Elmer, Optima 5300DV).

2.4. Catalytic degradation of contaminants

The catalytic degradation tests were carried out in a 100 mL beaker at 20 ± 2 °C. In each run, 5 mg of catalyst was suspended in a 50 mL of the pH-buffered solutions (pH 7, 10 mM phosphate buffer), containing a target compound in a given concentration (i.e., [RhB] = 100 mg/L, [ATZ] = [SMX] = [4-CP = [BPS] = [BPF] = 10 mg/L, [FFA] = 0.1 mM). Then, PMS (C_o = 0.35 mM) was added into the solution to trigger the degradation reaction. At each time interval, the reaction solution (0.5 mL) was withdrawn, filtered and quenched with excess pure methanol (1.5 mL). The RhB concentration was determined at the absorption peak of 554 nm on a UV–Vis spectrophotometer (Hach, DR5000). The concentrations of other organic contaminants were analyzed using an ACQUITY UHPLC with a BEH C18 column (1.0 × 50 mm, 1.7 μm). Detailed analysis conditions are shown in Table S1. Residual cobalt concentrations were measured by the ICP-OES (Perkin Elmer, Optima 5300DV). Electron paramagnetic resonance spectroscopy (EPR, Bruker A200 spectrometer, Germany) was applied

to in situ investigate the generation of reactive radicals. Hydroxyl radical reactions were performed as follows: 5 mg of the catalyst was suspended in 50 mL aqueous solution containing 2 mM NaOH and 0.5 mM terephthalic acid. Then, PMS was added under stirring. At each time interval, the fluorescence signals of the solutions were measured by a fluorescence spectrophotometer (Hitachi, F7000). The excitation light wavelength used in recording fluorescence spectra was 315 nm.

3. Results and discussion

3.1. Design, synthesis and characterizations of catalysts

Inspired by the homogeneous catalysis, we conceived that the cobalt sites can serve as the atomic nodes for constructing the bulk structure of supported Co catalysts. As such, the active cobalt centers can be homogeneously dispersed into the entire catalysts, which is distinctly different from other Co-supported catalysts that the aggregated/larger cobalt oxide NPs randomly distributed on the surface of the supported materials. To implement above assumption, cobalt silicate hydroxide ($Co_3(Si_2O_5)_2(OH)_2$, abbreviated as CSH) was selected as the target cobalt compound. This is because (1) CSH can be easily fabricated by a simple hydrothermal reaction; (2) cobalt in the CSH can serve as the isolated active site to be homogeneously dispersed into the bulk catalyst at an atomic scale. On the other hand, the architecture of hierarchically hollow nanospheres assembled by ultrathin nanosheets can be a good candidate to maximize the exposure of the cobalt site, owing to its high SSA and excellent structural stability.

Herein, a facile dissolution-regrowth strategy was developed for controllable synthesis of the CSH (Fig. 1). Monodisperse SiO_2 nanospheres with an average diameter of 118 nm (Figure S1) were used as silicic precursor and structural template. Cobalt(III) acetylacetonate (Co(acac)$_3$) was selected as a cobaltic precursor as Co(acac)$_3$ has a better adsorption affinity toward SiO_2 nanospheres and better stability as compared with inorganic cobalt salts [18]. Under the hydrothermal conditions, SiO_2 nanospheres have been slowly dissolved to generate the silicate anions [18] and Co(acac)$_3$ molecules were adsorbed on the SiO_2 surface, which were decomposed simultaneously to release the cobalt cations. Then the reaction between the silicate anions and cobalt cations will initiate. The obtained CSH was deposited on the surface of SiO_2 spheres, forming a SiO_2@CSH core-shell nanostructure. During the hydrothermal reaction, morphology evolved from the core-shell nanostructure to yolk-shell nanostructure due to the dissolution of SiO_2 core and the simultaneous growth of the CSH shell. With further prolongation of the reaction time, a unique hierarchical hollow nanoarchitecture can be finally obtained.

Fig. 2 shows typical TEM images of the as-synthesized CSH with different dosage of SiO_2. When 20 mg SiO_2 was added, the resulting CSH is shown as mesoporous nanospheres with an average size of 226 nm (Fig. 2a). With a closer examination, the mesoporous nanospheres are compactly assembled by ultrathin nanosheets with an average thickness of 3 nm (Fig. 2e). Interestingly, when SiO_2 dosage increased to 40 mg, the mesoporous CSH nanospheres have evolved into hierarchical hollow CSH nanospheres (Fig. 2b). High magnification TEM image shows that the thickness of the hollow shell is 29 nm (Fig. 2f). Such obvious morphological evolution may be attributed to the different reaction kinetics between the dissolution of SiO_2 and the regrowth of CSH, which are synchronously controlled by the dosage of SiO_2. As the SiO_2 dosage was further increased to 60 mg, the unique hierarchical hollow nanoarchitecture of CSH remains unchanged (Fig. 2c). But the thickness of the shell has decreased to 20 nm (Fig. 2g). Moreover, the shell thickness further decreased to 11 nm when the SiO_2 dosage reached 80 mg (Fig. 2d and h). The significant mismatches between the mass ratio of SiO_2 and Co(acac)$_3$ possibly hindered the generation of CSH, thus leading to the formation of thicker shells. Besides, two “halo” rings corresponding to the (2 1 0) and (3 3 0) planes of CSH (PDF#210871) can be discerned in the selected-area electron diffraction (SAED) images for all the CSH samples (Fig. 2i-L). These results indicate that the crystallinity of the CSHs is not high. However, the lower crystallinity has been reported to possibly improve the activity in catalytic degradation [19,20].

The crystallographic phase of CSH was further examined by XRD. All of the weak reflection peaks in Fig. 3a can be readily indexed to a pure hexagonal phase (PDF #210871). Two diffraction peaks around at 35° and 60° are attributed to the (2 1 0) and (3 3 0) planes of CSH, respectively. The relative weak intensities of the diffraction peaks suggest that the crystallinities of CSHs are poor, which are consistent with these observations in SAED patterns. XPS full survey spectra (Figure S2) reveal that all the as-synthesized CSH samples contain Si, O, and Co elements with characteristic peaks at binding energies of 101.7 (Si 2p), 530.4 (O 1 s), and 780.6 eV (Co 2p), respectively. The Co 2p fine spectra of the as-synthesized CSH (Fig. 3b) show two main peaks at binding energies of 780.1 and 796.1 eV, along with two satellite peaks at 785.8

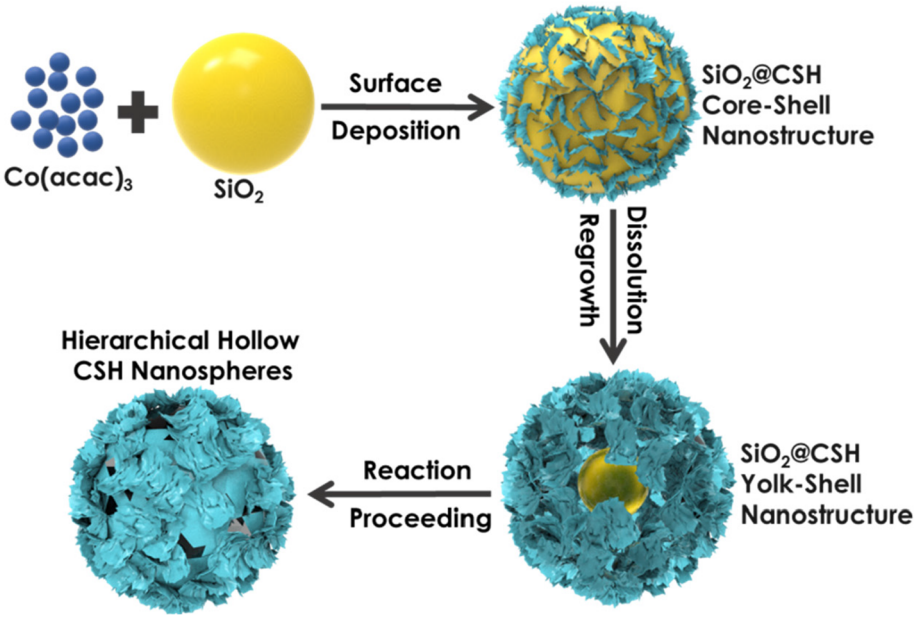

Fig. 1. Schematic illustration of the synthesis of hierarchical hollow CHS nanospheres.

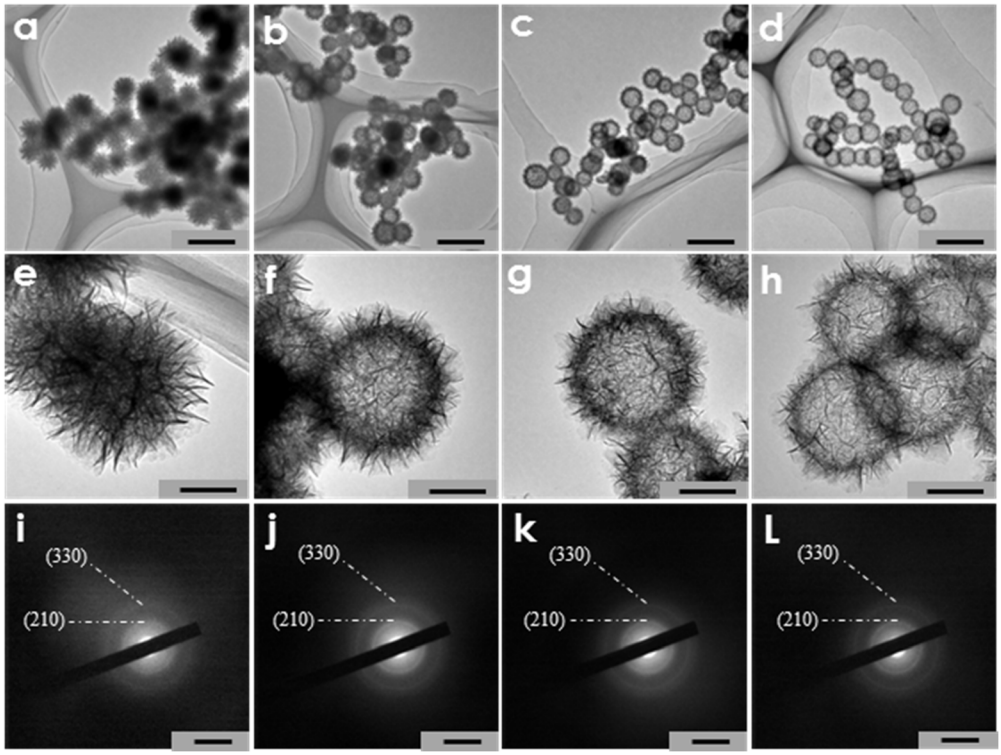

Fig. 2. Low magnification TEM images of (a) CSH-20, (b) CSH-40, (c) CSH-60 and (d) CSH-80. Scale bars: 500 nm. High magnification TEM images of (e) CSH-20, (f) CSH-40, (g) CSH-60 and (h) CSH-80. Scale bars: 100 nm. SAED patterns of (i) CSH-20, (j) CSH-40, (k) CSH-60 and (L) CSH-80. Scale bars: 5 1/nm.

and 802.5 eV. The positions of these peaks and their separation are ascribed to Co^{2+} species in Co-O-Si [21]. In addition, the difference in binding energy of about 6 eV for main and satellite peaks is relatively lower than that of CoO (9.5 eV) [22], demonstrating the absence of CoO in the as-synthesized CSH.

The bonding characteristics of functional groups on the as-prepared CSH were further identified by FTIR (Fig. 3c). The peaks at 3488 and 1628 cm^{-1} are attributed to the OH bending vibration of adsorbed molecular water. A sharp smaller peak at 3628 cm^{-1} is ascribed to the OH stretching mode of Co talc structure [23]. A peak at 1020 cm^{-1} is

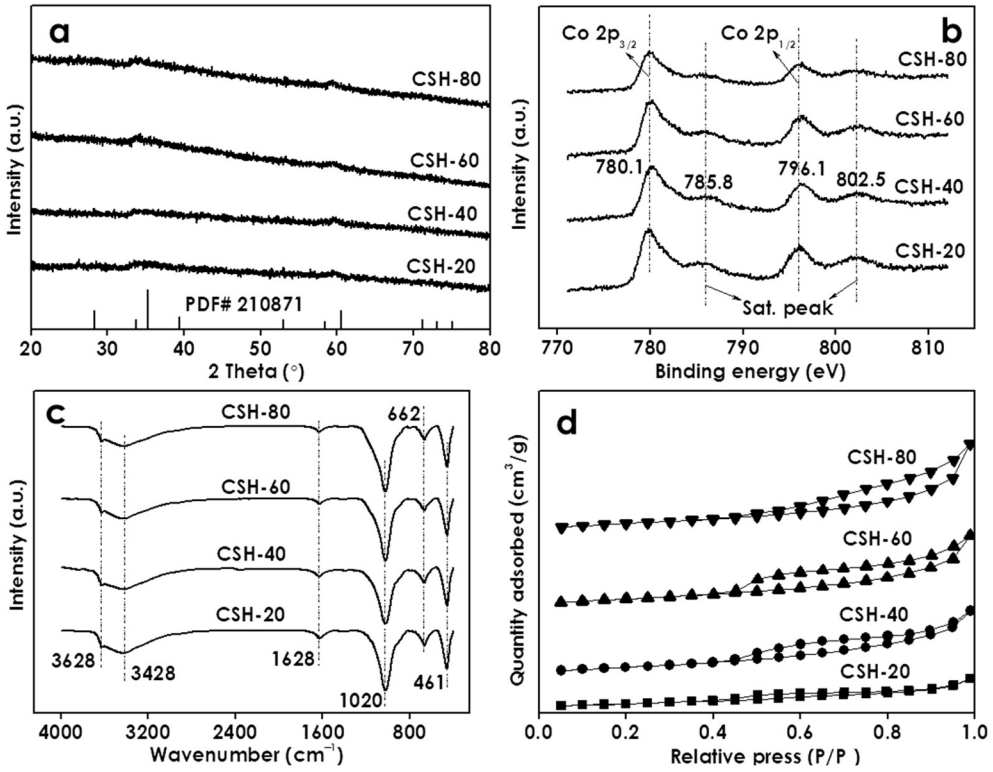

Fig. 3. XRD patterns (a), Co 2p fine XPS spectra (b), FTIR spectra (c) and N_2 adsorption-desorption isotherms (d) of the samples.

attributed to the Si–O–Co bond formed by the reaction between silicate anions and cobalt cations [24]. In addition, there are two signals at 662 and 461 cm^{-1}, which can be assigned to Si–O–Si rocking and Si–O–Co bending vibrations, respectively [25,26]. Similar to the XPS results, the characteristic peak at 578 cm^{-1} corresponding to the Co–O stretching vibrations of CoO [21] can not be found in the FTIR spectra, further confirming the absence of CoO in the as-synthesized samples.

Fig. 3d shows that N_2 adsorption-desorption isotherms of CSH exhibit a typical type H2 of IV isotherm curve that is characteristic feature of mesoporous structure. Their pore diameters are similar at 3.8 nm. The calculated SSAs of CSH-20, CSH-40, CSH-60, and CSH-80 are 346, 479, 485, and 492 m^2/g, respectively (Table S2). Their corresponding pore volumes are 0.54, 1.24, 1.42, and 1.63 cm^3/g, respectively. Obviously, the morphological evolution from mesoporous nanospheres to hierarchical hollow nanospheres leads to the significant increases in SSA and pore volume. A flat increasing tendency can be observed with the decrease of shell thickness. Moreover, ICP-OES shows that the cobalt contents of CSH-20, CSH-40, CSH-60 and CSH-80 are 27.6, 28.8, 27.0, and 23.1%, respectively (Table S2).

3.2. Catalytic activity and stability

The catalytic activities of the as-synthesized CSH were preliminarily evaluated in activation of PMS for degradation of RhB, a typical non-biodegradable dye pollutant in textile wastewater. Fig. 4a shows that RhB is barely decomposed by PMS itself. Without PMS, a 22% of RhB can be eliminated by physical adsorption on CSH-20 (Figure S3). The adsorption capacity of CSH-20 is slightly lower than that of other CSHs (26%) due to its lower SSA. When both PMS and CSH-20 were added, 73% of RhB can be degraded within 20 min, indicating that CSH-20 can activate PMS to generate massive reactive species for RhB degradation. In contrast, only 28, 21 and 2% of RhB can be degraded by $Co(OH)_2$, Co_3O_4 NPs and CuO NPs, respectively. Moreover, 78, 83 and 78% of RhB degradation can be achieved by CSH-40, CSH-60 and CSH-80, respectively, highlighting the excellent performance of CHS in PMS activation for pollutant degradation.

Cobalt leaching of the as-synthesized CSH was investigated by ICP-OES. Fig. 4b shows that the residual cobalt concentration of CSH-20@PMS system is 0.51 mg/L, lower than the emission standard of industrial wastewater (1.0 mg/L) based on GB/T 25467-2010 of China. Interestingly, when the hierarchical hollow CSH-40 nanospheres were added, the cobalt leaching rapidly declined from 0.51 to 0.24 mg/L. More importantly, with the decrease of hollow shell thickness from 29 (CSH-40) to 11 nm (CSH-80), the cobalt concentration in the reaction system further reduced to 0.08 mg/L, which is below the maximum limits of drinking water (0.1 mg/L) enacted by US EPA [27]. The results demonstrate that the hierarchical hollow CSH-80 nanospheres with thinner shells manifest outstanding chemical stability.

To examine the structural stability, CSH-80 was further treated by mechanical grind. TEM image shows that the micro-morphology of CSH-80 is barely changed after the grinding (Figure S4). The catalytic activity of the ground CSH-80 remains unchanged as compared to the original CSH-80 (Figure S5). The durability of CSH-80 was evaluated by the cyclic degradation test. Fig. 4c displays that only 5% decrease in RhB removal efficiency was observed in the 2nd run. Then the removal efficiencies of RhB were stabilized at around 70% in the 3rd to 5th runs. This result indicates that the CSH-80 presents an excellent reusability. However, when the CSH-80 has undergone 10 runs, the removal efficiency of RhB has declined to 48% (Figure S6a). This is attributed to the collapse of hollow nanostructure and the loss of active cobalt, which are supported by the results of TEM (Figure S6b) and XPS (Figure S6c). Apart from the dye pollutant, six typical organic micro-pollutants including SMX, ATZ, 4-CP, FFA, BPS and BPF were employed to further evaluate the applicability of the CSH-80@PMS oxidative system. Fig. 4d

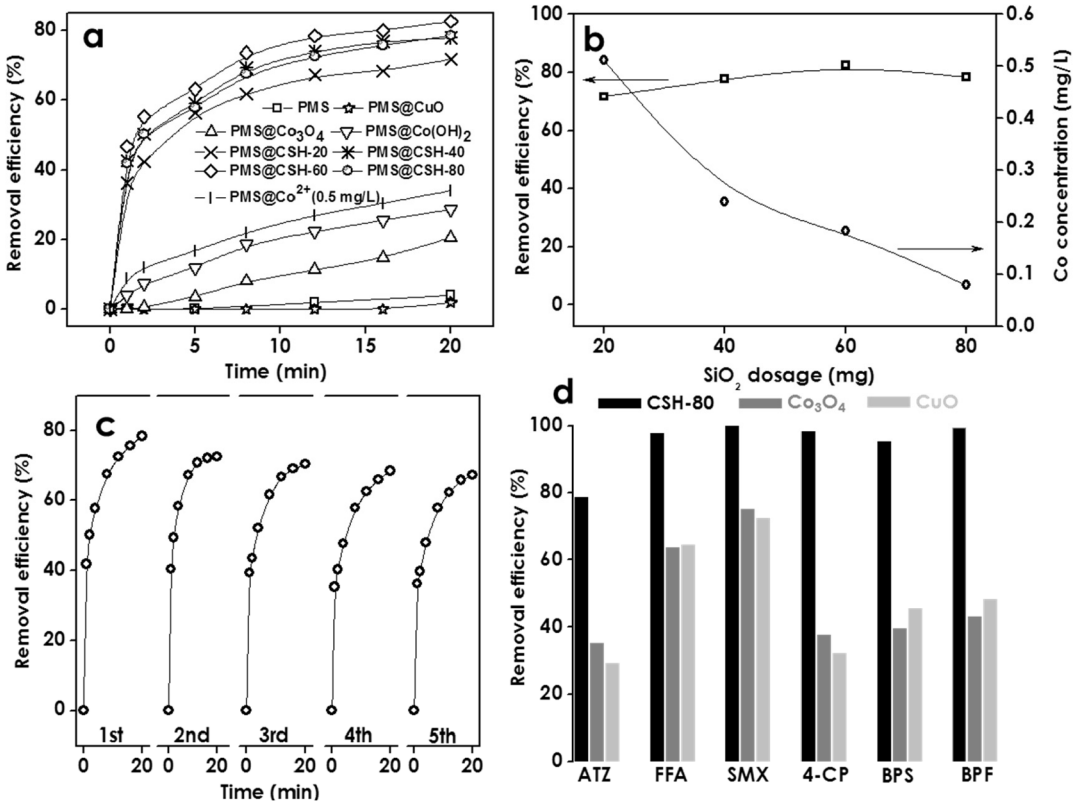

Fig. 4. Catalytic degradation of RhB on different catalysts (a); RhB removal efficiency and cobalt leaching concentration with change in the dosage of SiO_2 (b); RhB removal in repeated tests with the CSH-80 (c); catalytic degradation of six typical organic contaminants on the CSH-80 (d). Experimental condition: [catalyst] = 0.1 g/L, [RhB] = 100 mg/L, [PMS] = 0.35 mM, and pH = 7.

shows that all the organic micro-pollutants with different molecular structures can be efficiently decomposed in the CSHs-80@PMS system. Their degradation efficiency on CSH-80 is significantly higher than those of Co_3O_4 NPs and CuO NPs. Therefore, on the basis of the above-mentioned experimental results including contaminant degradation, cobalt leaching, physicochemical stability test, cyclic reuse and applicability test, it can be determined the hierarchical hollow CSH-80 nanospheres hold a great promise in remediation of wastewater containing diverse organic contaminants.

Further investigations were performed to explore the effect of reaction parameters on RhB degradation in the CSH-80@PMS system. Figure S7a shows the influence of initial RhB concentration on RhB degradation. With the initial RhB concentration increased from 60 to 100 mg/L, the degradation efficiency decreased from 95 to 78%. This could be attributed to the insufficient reactive radicals generated in the CSH-80@PMS system. Figure S7b shows that the increase of reaction temperature in a range of 20–40 °C produced a marginal effect on the degradation efficiency. The degradation rate was slightly enhanced by the raised temperature. Based on the Arrhenius equation, the activation energy of RhB oxidation by CSH-80@PMS was calculated to be 26.3 kJ/mol, which is much lower than that of other supported Co catalysts [28–31]. Similar to the previous observations [32,33], neutral or alkaline pH conditions are beneficial to the RhB degradation (Figure S7c). Figure S7d shows that high dosage of CSH-80 can improve the RhB degradation, because the higher catalyst loading can provide more active sites, thus facilitating the generation of more ROS for RhB degradation. In the same way, the increase of PMS dosage can also give a higher degradation rate (Figure S7e). Additionally, a limited inhibition of RhB oxidation can be observed in the presence of humic acid (a ubiquitous organic compound in the aquatic environment) with the concentrations in a range of 0–10 mg/L (Figure S7f). All these results demonstrate that the CSH-80@PMS system has an excellent adaptability under complicated water matrixes.

Encouraged by the above-mentioned results, actual contaminated water (Table S3) was employed to examine the practical application of CSH-80@PMS system. Around 80% of RhB can be degraded by the CSH-80@PMS system within 20 min (Fig. 5). In comparison, only a limited degradation of RhB was obtained by the Co_3O_4@PMS system (13%) and CuO@PMS system (16%). These exciting experiments suggest the great efficiency of the CSH-80@PMS oxidative system for remediation of actual wastewater.

3.3. Cobalt site efficiency of different Co-based catalysts

To evaluate the cobalt active sites of CSH-80, four typical supported Co catalysts (i.e., Al_2O_3@Co, P25@Co, SBA-15@Co and SiO_2@Co) have been synthesized for comparison. TEM images (Figure S8) show that the cobalt oxide NPs with irregular morphologies are severely aggregated in Al_2O_3@Co, P25@Co and SiO_2@Co. For SBA-15@Co, the larger cobalt oxide NPs are randomly dispersed on the surface of SBA-15 (Figure S8c). The aggregated or/and larger cobalt oxide NPs loaded on the supported materials can also be observed in previous studies [6,30,31,34,35]. The ICP-OES measurements indicate that the cobalt contents of Al_2O_3@Co, P25@Co, SBA-15@Co and SiO_2@Co are 15.4, 15.9, 15.0 and 15.1%, respectively (Table S3). The similar contents of cobalt in these Co-supported catalysts are attributed to the same amounts of cobalt precursor in the fabrication processes.

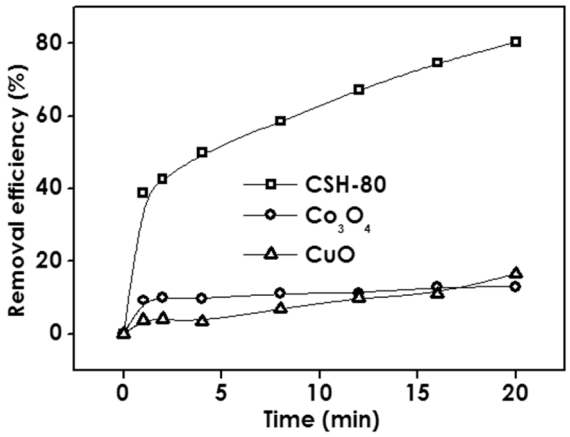

Fig. 5. Catalytic degradation of RhB in the actual water body. Experimental conditions: [catalyst] = 0.1 g/L, [RhB] = 100 mg/L, [PMS] = 0.35 mM, and pH = 7.

Fig. 6a shows that 78% of RhB can be efficiently degraded in the CSH-80@PMS reaction system. However, Al_2O_3@Co, P25@Co, SBA-15@Co and SiO_2@Co exhibited relative low catalytic activities, resulting in 17, 21, 26 and 16% of RhB degradation, respectively, which are much lower than that of CHS-80. The higher degradation efficiency achieved by the CSH-80 may be ascribed to its higher cobalt content (23%). Thus, to exclude the influence of cobalt content and explore the intrinsic catalytic activity of these Co-based materials, the degradation efficiencies were further normalized to the cobalt content (Fig. 6b). For the CSH-80, the normalized value was calculated to be 3.39, which still is 1.9, 2.5, 3.1 and 3.1 folds higher than that of the SBA-15@Co, P25@Co, Al_2O_3@Co and SiO_2@Co, respectively. In other words, 2.4 mol of cobalt in CSH-80 can give rise to the decomposition of 1.0 mol RhB; however, the decomposition of 1.0 mol RhB has required 4.6, 6.0, 7.4 and 7.4 mol of cobalt for the SBA-15@Co, P25@Co, Al_2O_3@Co and SiO_2@Co, respectively. This result features the high cobalt utilization efficiency in the CSH-80 on unit mass basis. Additionally, the normalized apparent rate constant of CHS-80 was calculated as 0.22 min^{-1}, which is 4.5, 5.9, 8.8 and 9.2 folds faster than those of SBA-15@Co, P25@Co, Al_2O_3@Co and SiO_2@Co (Fig. 6c), respectively, indicating the high catalytic oxidation rate of CSH-80@PMS system on unit mass basis. The intrinsic activity in the turnover frequency (TOF) per active site was estimated based on the assumption that every cobalt atom is catalytically active. It can be seen that the TOF of CHS-80 catalyzed RhB oxidation was calculated as 0.35 × 10^{-3} s^{-1}, which is 2.0, 2.6, 3.0 and 3.2 folds higher than that of the SBA-15@Co, P25@Co, Al_2O_3@Co and SiO_2@Co, respectively (Fig. 6d). This result demonstrated that CHS-80 had intrinsically much better activity than these conventional Co-based catalysts in activation of PMS for RhB degradation.

Different from the conventional Co-based catalysts for the overall efficiency of the materials, the design of CSH-80 aims at maximizing the cobalt active site in the heterogeneous catalysts. As such, high cobalt utilization efficiency, catalytic oxidation rate and TOF can be achieved in the CSH-80@PMS reaction system. To the best of our knowledge, this is the first time to develop the Co-based catalyst from the point of view of cobalt utilization efficiency in environmental catalysis, which may open a new window for designing high-performance Co-based catalysts toward future applications.

3.4. Catalytic oxidation mechanism

To unveil the contributions of reactive species in RhB degradation, classical radical quenching experiments were performed. Fig. 7a shows that the removal efficiency of RhB barely changed when the dosage of TBA (the scavenger of •OH radicals) [36] increased from 0 to 70 mM (the molar ratio of TBA:PMS is 200:1), demonstrating that •OH is not likely involved in the RhB degradation. When 7 mM methanol (the scavenger of $SO_4^{\bullet-}$/•OH radicals) [36] was added in the reaction system, the RhB degradation decreased from 78 to 67% (Fig. 7b). When the methanol dosage increased to 70 mM, the RhB removal further declined to 42%. This result indicates that $SO_4^{\bullet-}$ may be the major ROS responsible for the RhB degradation in CSH-80@PMS system. Fig. 7c shows that the addition of NaN_3, a scavenger of single oxygen ($^1O_2$) [7,11,36–38], can induce a significant decrease in RhB removal

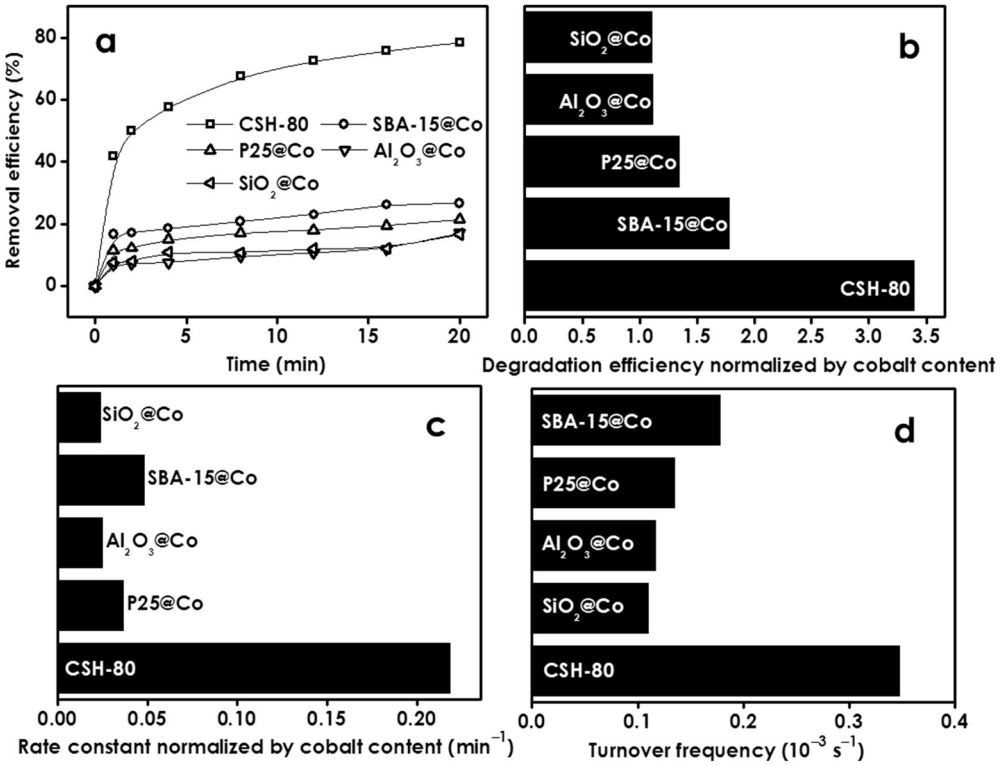

Fig. 6. Catalytic degradation of RhB on different Co-based catalysts (a), corresponding degradation efficiencies (b) and rate constants normalized by the cobalt content (c), and the turnover frequencies of catalysts (d). Experimental conditions: [catalyst] = 0.1 g/L, [RhB] = 100 mg/L, [PMS] = 0.35 mM, and pH = 7.

efficiency (from 78 to 32%). It should be pointed that the reaction rate constant for NaN_3 with $^1O_2$ [38] is as high as 1.0×10^9 M^{-1} s^{-1}, the rate constants for the NaN_3 with $SO_4^{\bullet-}$ [39] and •OH [40] can reach up to 2.52×10^9 M^{-1} s^{-1} and 1.2×10^{10} M^{-1} s^{-1}, respectively. Therefore, the decrease of RhB removal induced by the addition of NaN_3 cannot solidly support the significant contribution of $^1O_2$ in the RhB degradation.

To further identify the reactive species related to the RhB

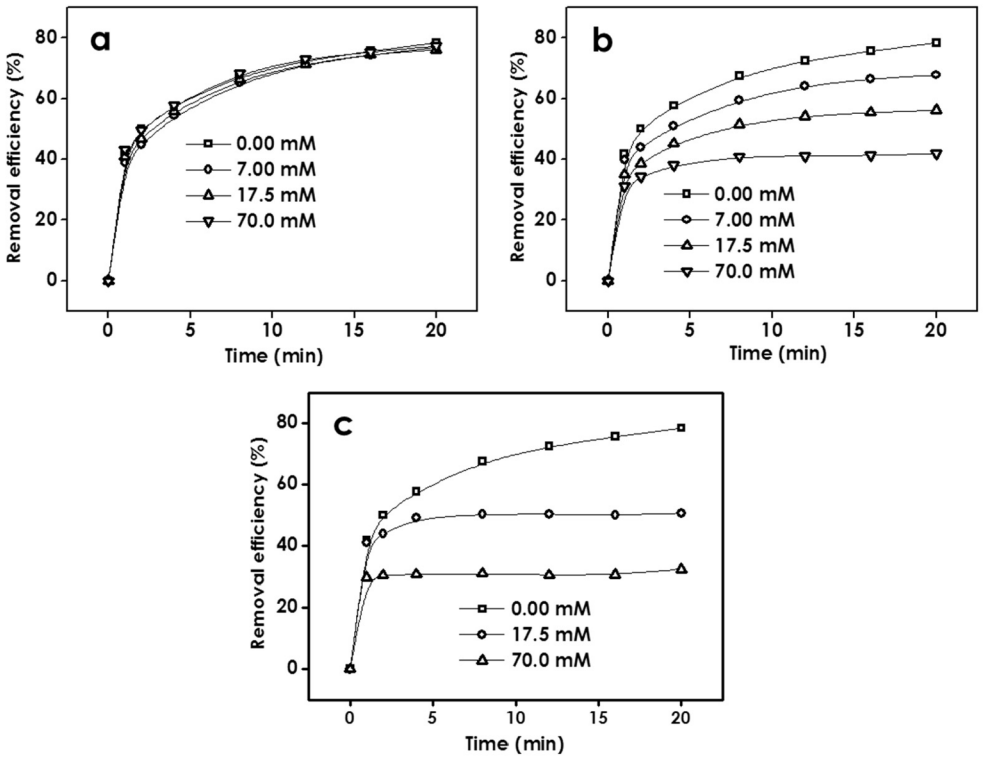

Fig. 7. Effects of TBA, methanol and NaN_3 on the catalytic degradation of RhB by the CSH-80. Experimental conditions: [CSH-80] = 0.1 g/L, [RhB] = 100 mg/L, [PMS] = 0.35 mM, [TBA] = [Methanol] = [NaN_3] = 0–70 mM, and pH = 7.

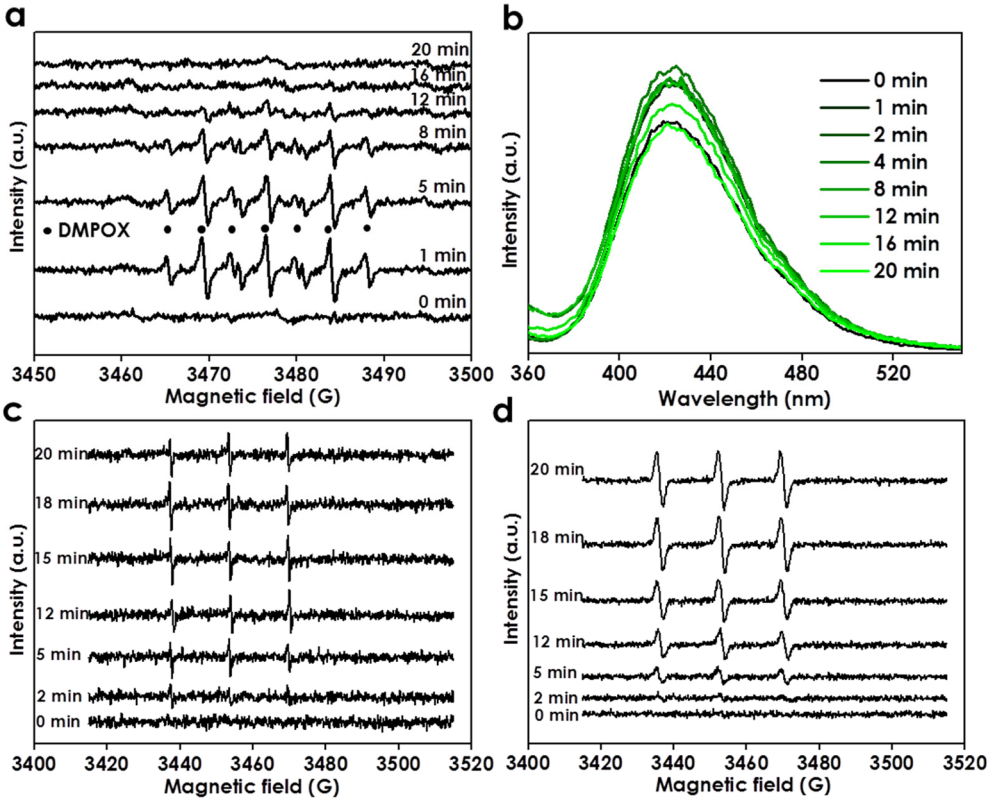

Fig. 8. EPR spectra obtained by spin trapping with DMPO (a), time-dependent fluorescence spectra of TAOH (b), EPR spectra obtained by spin trapping with TMP in the reaction system with (c) and without (d) CSH-80. Experimental conditions of EPR tests: [CSH-80] = 0.1 g/L, [RhB] = 100 mg/L, [PMS] = 0.35 mM, [DMPO] = 5.25 mM, [TMP] = 1 mM, and pH = 7.

degradation, in-situ EPR studies have been performed. DMPO was used as the spin trapping agent for detecting $SO_4^{\bullet-}$ and •OH. A control experiment shows that no radical adducts can be observed in the existence of PMS alone (Figure S9). However, a clear seven-line spectrum assigned to 5,5-dimethyl-2-oxo-pyrroline-1-oxyl (DMPOX) [41] has emerged in the presence of PMS and CSH-80 within 1 min (Fig. 8a). With the prolongation of reaction time, the signal of this spectrum became weak gradually. However, the characteristic signals of DMPO-$SO_4^{\bullet-}$ and DMPO-•OH do not appear during the whole reaction. According to the previous reports, DMPOX was generally produced by a secondary oxidation-reduction process in the interaction between strong oxidative species and DMPO [41,42]. In this reaction system, DMPOX may originate from the decomposition of the DMPO-$SO_4^{\bullet-}$ and DMPO-•OH adducts [43,44]. This is why the signals of DMPO-$SO_4^{\bullet-}$ and DMPO-•OH can be barely observed. The photoluminescence (PL) technology was also used for detection of •OH [45]. Fig. 8b shows that a fluorescent signal associated with 2-hydroxyterephthalic acid (TAOH, formed by the reaction of terephthalic acid with ·OH radicals) can be observed and its intensity increases at beginning and begins to decrease in the last period, similar to that of the DMPOX signal. This result suggests the presence of •OH radicals in the reaction system, which could be originated from the reaction between $SO_4^{\bullet-}$ and OH^-.

On the other hand, when TMP (the spin trapping reagent for $^1O_2$) was added, weak triplet EPR spectra corresponding to the oxidized TMP by $^1O_2$ can be observed (Fig. 8c) [7,41]. Surprisingly, a stronger and clearer signal of $^1O_2$ can also be found in the control experiment (i.e., without CSH-80) and its intensities have increased with the prolonged reaction time (Fig. 8d). However, the control experiment (Fig. 4a) suggests RhB is barely decomposed by PMS alone. In this regard, we can infer that a minor amount of $^1O_2$ may emerge in the reaction system whereas its contributions to RhB degradation can be neglected. Therefore, combined with all the evidences from quenching tests, EPR and PL studies, it can be concluded that $SO_4^{\bullet-}$, •OH and $^1O_2$ exist in the CSH-80@PMS system whereas $SO_4^{\bullet-}$ plays a substantial role in RhB degradation.

4. Conclusions

In summary, hierarchical hollow nanospheres of cobalt silicate hydroxide were successfully synthesized by a facile dissolution-regrowth approach. Owing to its unique design and elaborative nanoarchitecture, the active cobalt center can be homogeneously dispersed into the entire structure of the materials for adequate exposure of the cobalt center. In application of PMS activation and degradation of organic contaminants, the as-synthesized CSH-80 exhibited outstanding catalytic performance, excellent physicochemical stability and long-term durability. More importantly, the cobalt site of CSH-80 was much higher than those of the conventional Co-based catalysts in activation of PMS for contaminant degradation. Correspondingly, the TOF of CSH-80 catalyzed RhB oxidation was 2.0–3.2 folds higher than that of the supported cobalt catalysts. We expect that this design philosophy of maximizing utilization of cobalt will provide new opportunities for the future development of high-performance cobalt-based heterogeneous catalysts for environmental remediation.

Acknowledgements

This work was supported by the National Natural Science Foundation of China (No. 51678187 and 51678285), the National Key Research and Development Program of China (No. 2018YFC0406405), the“5511” Innovative Research Team of Science and Technology of Jiangxi Province (No. 20165BCB19008), the Key Project of Science and Technology of Jiangxi Province (No. 20173ABC28010), and Science and Technology Project of the Education Department of Jiangxi Province (No. GJJ170620).

Appendix A. Supplementary data

Supplementary data to this article can be found online at https://doi.org/10.1016/j.cej.2018.11.121.

References

[1] X. Duan, H. Sun, S. Wang, Metal-free carbocatalysis in advanced oxidation reactions, Acc. Chem. Res. 51 (2018) 678–687.
[2] S. Wang, J. Tian, Q. Wang, Z. Zhao, F. Cui, G. Li, Low-temperature sintered high-strength CuO doped ceramic hollow fiber membrane: Preparation, characterization and catalytic activity, J. Membrane. Sci. 570–571 (2019) 333–342.
[3] M. Antonopoulou, E. Evgenidou, D. Lambropoulou, I. Konstantinou, A review on advanced oxidation processes for the removal of taste and odor compounds from aqueous media, Water Res. 53 (2014) 215–234.
[4] M.A. Oturan, J.J. Aaron, Advanced oxidation processes in water/wastewater treatment: principles and applications: a review, Rev. Environ. Sci. Technol. 44 (2014) 2577–2641.
[5] G. Liu, S. You, Y. Tan, N. Ren, In situ photochemical activation of sulfate for enhanced degradation of organic pollutants in water, Environ. Sci. Technol. 51 (2017) 2339–2346.
[6] P. Hu, M. Long, Cobalt-catalyzed sulfate radical-based advanced oxidation: a review on heterogeneous catalysts and applications, Appl. Catal., B 181 (2016) 103–117.
[7] P. Shao, J. Tian, F. Yang, X. Duan, S. Gao, W. Shi, X. Luo, F. Cui, S. Luo, S. Wang, Identification and regulation of active sites on nanodiamonds: establishing a highly efficient catalytic system for oxidation of organic contaminants, Adv. Funct. Mater. 28 (2018) 1705295.
[8] C. Su, X. Duan, J. Miao, Y. Zhong, W. Zhou, S. Wang, Z. Shao, Mixed conducting perovskite materials as superior catalysts for fast aqueous-phase advanced oxidation: a mechanistic study, ACS Catal. 7 (2017) 388–397.
[9] X. Duan, H. Sun, Y. Wang, J. Kang, S. Wang, N-doping-induced nonradical reaction on single-walled carbon nanotubes for catalytic phenol oxidation, ACS Catal. 5 (2015) 553–559.
[10] Y. Ahn, E. Yun, J. Seo, C. Lee, S. Kim, J. Kim, J. Lee, Activation of peroxymonosulfate by surface-loaded noble metal nanoparticles for oxidative degradation of organic compounds, Environ. Sci. Technol. 50 (2016) 10187–10197.
[11] H. Lee, H. Kim, S. Weon, W. Choi, Y. Hwang, J. Seo, C. Lee, J. Kim, Activation of persulfates by graphitized nanodiamonds for removal of organic compounds, Environ. Sci. Technol. 50 (2016) 10134–10142.
[12] G.P. Anipsitakis, D.D. Dionysiou, Degradation of organic contaminants in water with sulfate radicals generated by the conjunction of peroxymonosulfate with cobalt, Environ. Sci. Technol. 37 (2003) 4790–4797.
[13] J. Li, Y. Yi, P. Shi, Q. Wang, D. Li, H. Asif, M. Yang, Facile Synthesis of graphene-cobalt hydroxide nanocomposite and application in degradation of acid orange 7, Acta Phys.-Chim. Sin. 30 (2014) 1720–1726.
[14] L. Hu, X. Yang, S. Dang, An easily recyclable Co/SBA-15 catalyst: heterogeneous activation of peroxymonosulfate for the degradation of phenol in water, Appl. Catal., B 102 (2011) 19–26.
[15] Z. Zhu, L. Zhong, Z. Zhang, H. Li, W. Shi, F. Cui, W. Wang, Gravity driven ultrafast removal of organic contaminants across catalytic superwetting membranes, J. Mater. Chem. A 5 (2017) 25266–25275.
[16] T. Zeng, X. Zhang, S. Wang, H. Niu, Y. Cai, Spatial confinement of a Co_3O_4 catalyst in hollow metal-organic frameworks as a nanoreactor for improved degradation of organic pollutants, Environ. Sci. Technol. 49 (2015) 2350–2357.
[17] Y. Yao, C. Xu, S. Miao, H. Sun, S. Wang, One-pot hydrothermal synthesis of $Co(OH)_2$ nanoflakes on graphene sheets and their fast catalytic oxidation of phenol in liquid phase, J. Colloid Interface Sci. 402 (2013) 230–236.
[18] P. Shao, J. Tian, W. Shi, Y. Yang, X. Yang, S. Gao, F. Cui, Programmable synthesis of metal hydroxide/oxide hollow architectures: towards an efficient and robust photocatalyst for water remediation, J. Mater. Chem. A 5 (2017) 124–132.
[19] P. Shao, X. Duan, J. Xu, J. Tian, W. Shi, S. Gao, M. Xu, F. Cui, S. Wang, Heterogeneous activation of peroxymonosulfate by amorphous boron for degradation of bisphenol S, J. Hazard. Mater. 322 (2017) 532–539.
[20] P. Shao, J. Tian, Z. Zhao, W. Shi, S. Gao, F. Cui, Amorphous TiO_2 doped with carbon for visible light photodegradationof rhodamine B and 4-chlorophenol, Appl. Surf. Sci. 324 (2015) 35–43.
[21] M. Domínguez, E. Taboada, H. Idriss, E. Molinsc, J. Llorca, Fast and efficient hydrogen generation catalyzed by cobalt talc nanolayers dispersed in silica aerogel, J. Mater. Chem. 20 (2010) 4875–4883.
[22] F. Mueller, D. Bresser, N. Minderjahn, J. Kalhoff, S. Menne, S. Krueger, M. Winter, S. Passerini, Cobalt orthosilicate as a new electrode material for secondary lithium-ion batteries, Dalton Trans. 43 (2014) 15013–15021.
[23] R. Al-Oweini, H. El-Rassy, Synthesis and characterization by FTIR spectroscopy of silica aerogels prepared using several $Si(OR)_4$ and $R''Si(OR')_3$ precursors, J. Mol. Struct. 919 (2009) 140–145.
[24] H. Cui, M. Zayat, D. Levy, Effect of HCl on the PPO assisted sol-gel synthesis of olivine-type Co_2SiO_4 ultrafine particles, J. Sol-Gel Sci. Technol. 40 (2006) 83–87.
[25] G. Ortega-Zarzosa, C. Araujo-Andrade, M.E. Compean-Jasso, J.R. Martínez, F. Ruiz, Cobalt oxide/silica xerogels powders: x-ray diffraction, infrared and visible absorption studies, J. Sol-Gel Sci. Technol. 24 (2002) 23–29.
[26] J.T. Kloprogge, M. Hammond, L. Hickey, R.L. Frost, Low temperature synthesis of cobalt clays, J. Mater. Sci. Lett. 21 (2002) 931–933.
[27] W. Qiu, Y. Zheng, Removal of lead, copper, nickel, cobalt, and zinc from water by a cancrinite-type zeolite synthesized from fly ash, Chem. Eng. J. 145 (2009) 483–488.
[28] P. Shukla, H. Sun, S. Wang, H.M. Ang, M.O. Tadé, Co-SBA-15 for heterogeneous oxidation of phenol with sulfate radical for wastewater treatment, Catal. Today 175 (2011) 380–385.
[29] H. Sun, H. Tian, Y. Hardjono, C.E. Buckley, S. Wang, Preparation of cobalt/carbon-xerogel for heterogeneous oxidation of phenol, Catal. Today 186 (2012) 63–68.
[30] P. Shukla, S. Wang, K. Singh, H.M. Ang, M.O. Tadé, Cobalt exchanged zeolites for heterogeneous catalytic oxidation of phenol in the presence of peroxymonosulphate, Appl. Catal., B 99 (2010) 163–169.
[31] P. Shukla, H. Sun, S. Wang, H.M. Ang, M.O. Tadé, Nanosized Co_3O_4/SiO_2 for heterogeneous oxidation of phenolic contaminants in waste water, Sep. Purif. Technol. 77 (2011) 230–236.
[32] T. Zhang, H. Zhu, J.P. Croué, Production of sulfate radical from peroxymonosulfate induced by a magnetically separable $CuFe_2O_4$ spinel in water: efficiency, stability, and mechanism, Environ. Sci. Technol. 47 (2013) 2784–2791.
[33] Y. Feng, D. Wu, Y. Deng, T. Zhang, K. Shih, Sulfate radical-mediated degradation of sulfadiazine by $CuFeO_2$ rhombohedral crystal-catalyzed peroxymonosulfate: synergistic effects and mechanisms, Environ. Sci. Technol. 50 (2016) 3119–3127.
[34] P. Shukla, H. Sun, S. Wang, H.M. Ang, M.O. Tadé, Activated carbon supported cobalt catalysts for advanced oxidation of organic contaminants in aqueous solution, Appl. Catal., B 100 (2010) 529–534.
[35] W. Zhang, H.L. Tay, S.S. Lim, Y. Wang, Z. Zhong, R. Xu, Supported cobalt oxide on MgO: highly efficient catalysts for degradation of organic dyes in dilute solutions, Appl. Catal., B 95 (2010) 93–99.
[36] Y. Zhou, J. Jiang, Y. Gao, J. Ma, S. Pang, J. Li, X. Lu, L. Yuan, Activation of peroxymonosulfate by benzoquinone: a novel nonradical oxidation process, Environ. Sci. Technol. 49 (2015) 12941–12950.
[37] M.Y. Li, C.S. Cline, E.B. Koker, H.H. Carmichael, C.F. Chignell, P. Bilski, Quenching of singlet molecular oxygen ($^1O_2$) by azide anion in solvent mixtures, Photochem. Photobiol. 74 (2001) 760–764.
[38] H.E. Gsponer, C.M. Previtali, N.A. Garcí, Kinetics of the photosensitized oxidation of polychlorophenols in alkaline aqueous solution, Toxicol. Environ. Chem. 16 (1987) 23–37.
[39] R.E. Huie, C.L. Clifton, Temperature dependence of the rate constants for reactions of the sulfate radical, SO_4^-, with anions, J. Phys. Chem. 94 (1990) 8561–8567.
[40] G.V. Buxton, C.L. Greenstock, W.P. Helman, A.B. Ross, Critical review of rate constants for reactions of hydrated electrons, hydrogen atoms and hydroxyl radicals ($\cdot OH/\cdot O^-$ in aqueous solution, J. Phys. Chem. Ref. Data 17 (1988) 513–886.
[41] Y. Wang, D. Cao, X. Zhao, Heterogeneous degradation of refractory pollutants by peroxymonosulfate activated by CoO_x-doped ordered mesoporous carbon, Chem. Eng. J. 328 (2017) 1112–1121.
[42] C. Bernofsky, B.M.R. Bandara, O. Hinojosa, Electron-spin-resonance studies of the reaction of hypochlorite with 5,5-dimethyl-1-pyrroline-N-oxide, Free Radic. Biol. Med. 8 (1990) 231–239.
[43] K. Ranguelova, A.B. Rice, A. Khajo, M. Triquigneaux, S. Garantziotis, R.S. Magliozzo, R.P. Mason, Formation of reactive sulfite-derived free radicals by the activation of human neutrophils: an ESR study, Free Radic. Biol. Med. 52 (2012) 1264–1271.
[44] S. Maeno, Q.Q. Zhu, M. Sasaki, T. Miyamoto, M. Fukushima, Monopersulfate oxidation of tetrabromobisphenol A by an iron(III)-phthalocyaninetetrasulfate catalyst coordinated to imidazole functionalized silica particles, J. Mol. Catal. A: Chem 400 (2015) 56–63.
[45] P. Shao, J. Tian, B. Liu, W. Shi, S. Gao, Y. Song, M. Ling, F. Cui, Morphology-tunable ultrafine metal oxide nanostructures uniformly grown on graphene and their applications in the photo-Fenton system, Nanoscale 7 (2015) 14254–14263.